arXiv:1606.06416v1 [cond-mat.mes-hall] 21 Jun 2016

Non-equilibrium fractional quantum Hall states visualized by optically detected MRI

John N. Moore,[1] Junichiro Hayakawa,[1] Takaaki Mano,[2] Takeshi Noda,[2] and Go Yusa[1,*]

[1] *Department of Physics, Tohoku University, Sendai 980-8578, Japan*
[2] *National Institute for Materials Science, Tsukuba, Ibaraki 305-0047, Japan*

(Dated: June 22, 2016)

Using photoluminescence microscopy enhanced by MRI, we visualize in real space both electron and nuclear polarization occurring in non-equilibrium FQH liquids. We observe stripe-like regions comprising FQH excited states which discretely form when the FQH liquid is excited by a source-drain current. These regions are topologically protected and deformable, and give rise to bidirectionally polarized nuclear spins as spin-resolved electrons flow across their boundaries.

PACS numbers: 73.43.-f, 78.67.-n, 76.60.-k, 42.30.-d

The study of nuclear spins in semiconductor materials has become increasingly relevant as both a tool for probing the properties of electrons in semiconductors [1–12], and a means for developing understanding of quantum information processing [13–18]. These studies were enabled by unconventional nuclear magnetic resonance (NMR) in which nuclear polarization is detected via resistance or optical response of samples, i.e. resistively or optically detected NMR.

In particular, resisitively detected NMR has been a powerful tool for studying fractional quantum Hall (FQH) states [7–12]. FQH states form in a strongly interacting 2D electron system under a perpendicular magnetic field at fractional values of the Landau level filling factor ν [19]. The FQH state is a type of topological state of matter, and owes its energetic stability to its boundaries, i.e. edge states, which exist between the bulk state and the surrounding vacuum [20]. In the trivial case, e.g., $\nu = 1/3$, the 2D bulk of FQH states is gapped by electron-spin- (Zeeman energy) and Coulomb-interaction-induced energy gaps [19]. However, there also are non-trivial FQH states, e.g. $\nu = 2/3$, for which the gap can be closed at a certain critical magnetic field $B_{\rm C}$ under which the non-magnetic (unpolarized) and perfect ferromagnetic (polarized) phases, corresponding to electron spin polarizations P of 0 and 1, respectively, are degenerate; this leads to a first-order phase transition and the formation of magnetic domains [21]. For ν slightly lower (higher) than 2/3, the ferromagnetic (non-magnetic) phase becomes the ground state.

Near the phase transition, it is known that longitudinal resistance R_{xx} is dramatically increased in response to a large source-drain current [7–12, 15] bringing the system out of equilibrium. This R_{xx} enhancement is understood in conjunction with the nuclear spin polarization $P_{\rm N}$, as confirmed by resistively detected NMR[8]. However, the underlying mechanism behind the R_{xx} enhancement and the associated $P_{\rm N}$ has been unknown for decades despite its importance and versatility. In this Letter, we examine the origins of this intriguing effect in relation to the topological stability of the non-equilibrium FQH state. Using photoluminescence (PL) microscopy enhanced by magnetic resonance imaging (MRI), we visualize in real space both electron and nuclear polarization occurring in non-equilibrium FQH liquids. In response to a perturbation, we show the discrete transformation of the topologically protected FQH liquid into stripe-like regions comprising FQH excited states. These regions constitute topologically protected structures across which spin-resolved electrons flow to generate bidirectionally polarized nuclear spins. These findings demonstrate powerful and sensitive microscopic visualization tools for exploring spin-related phenomena and furthering understanding of semiconductor physics.

First, we confirmed the previously reported R_{xx} enhancement using a 15-nm-wide GaAs/AlGaAs quantum well (QW) sample containing a FQH liquid [22]. Under the small perturbation of an alternating source-drain current $I_{\rm SD}$ (2 nA, 13 Hz) at approximately $B_{\rm C}$, $\nu = 2/3$, R_{xx} becomes low [Fig. 1(a), green line] with a small peak due to the phase transition[7, 8]. In contrast, under large perturbation ($I_{\rm SD}$ = 120 nA), R_{xx} is dramatically increased in the steady state [Fig. 1(a), red line], similar to previous reports [7–12, 15].

Under these non-equilibrium conditions we obtained real-space images of FQH liquids [Figs. 1(b)−1(f)] under varied $I_{\rm SD}$-induced perturbations at $B = B_{\rm C} = 6.8$ T via polarization-sensitive scanning optical microscopy and spectroscopy of the sample's PL [21, 22]. The PL intensity from the singlet charged excitons [23, 24] used to construct these images is primarily anti-correlated with the local P [21]. Therefore, non-magnetic and ferromagnetic phases are distinguished by strong and weak PL intensities, respectively [21]. Because the ground state at $\nu = 0.660$ ($< 2/3$) is a ferromagnetic phase, the PL of the entire region is uniformly low (blue) for low perturbation [$I_{\rm SD} \leq 30$ nA; Figs. 1(b) and 1(c)]. Gapless edge channels at the bulk-vacuum interface protect the gapped bulk FQH liquid, although its electrochemical potential is far from equilibrium owing to the Hall voltage, $V_{\rm H}$. For high perturbation, high-PL-intensity regions (red) appear (determined to indicate a non-magnetic phase based on their spectra [21]) and bridge both sides of the sample. Importantly, these stripe-shaped structures comprising the

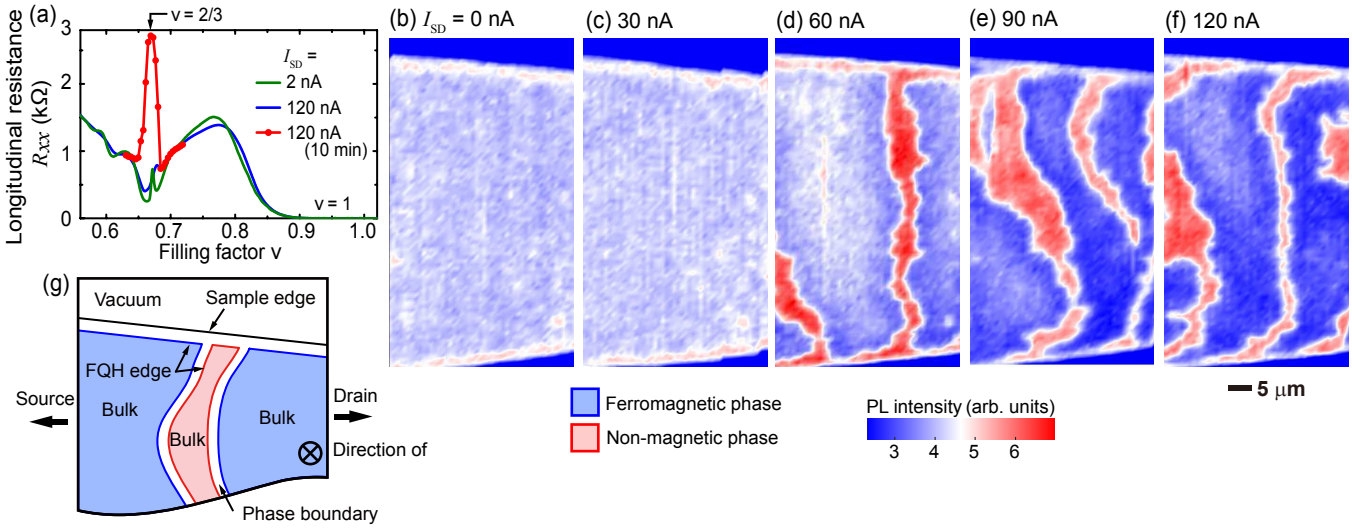

FIG. 1. (Color online) (a) Longitudinal resistance R_{xx} as function of ν. (Green) $I_{\rm SD} = 2$, (blue, red) 120 nA. ν is scanned over $0.5 - 1.02$ with 3.15×10^{-4} /s (green, blue) and 6.18×10^{-6} /s (red) scan speed. (b) to (f) 38× 68-μm^2 spatial images showing PL intensity of charged exciton singlet peak (PL intensity), at $\nu = 0.660$ with $I_{\rm SD}$ (Hall voltage, $V_{\rm H} = \frac{3}{2G_0} I_{\rm SD}$, G_0: quantized conductance) of: (b) 0 (0); (c) 30 (1.16); (d) 60 (2.32); (e) 90 (3.48); and (f) 120 nA (4.65 meV). $T \sim 60$ mK and $B = B_{\rm C} = 6.8$ T throughout unless otherwise specified [22]. (g) Schematic of observed images. The microscopic internal structure of the 2/3 edge state is not shown here, because it remains unclear [27, 28].

excited FQH liquid extend over a macroscopic scale and are topologically protected at their boundaries; because the boundary of two coexisting phases requires spin flips, the exchange interaction induces an energy barrier at the boundary [25], producing a new type of edge [Fig. 1(g)]. Through these exchange-interaction-induced edges, electrons injected from an electrode can return to the electrode (backscattering along the boundary), contributing to a non-zero R_{xx} [Fig. 1(a)].

This backscattering creates a local electrochemical potential difference across the two phases, generating potential steps at each phase boundary that descend monotonically in the direction opposing the conventional current. The reasonably well-reproducible stripe patterns [22] indicate that these potential steps are comparable to fluctuations in the sample's intrinsic random potential ($\sim$ 100 μeV [21, 22]). This, in turn, suggests that the backscattering rate at a boundary is $<\sim$ 0.1 using Landauer-Büttiker formalism [26], even without considering the internal structures of the ferromagnetic- and non-magnetic-phase 2/3 edge states, which remain unclear [27, 28]. Note that there are spin-resolved electrons flowing along the edges, and almost all the electrons must cross phase boundaries to contribute to $I_{\rm SD}$ (forward scattering across the boundary), with half undergoing spin flipping.

Such structures can be observed over a relatively wide range of $\nu = 2/3 \pm \sim 3\%$ [Figs. 2(a)−2(e)], unlike the phase transition ($\nu = 2/3 \pm \sim 0.3\%$[21]). At $\nu = 0.666$, the areas of the two phases are almost equal, owing to the phase transition [Fig. 2(d)], and the minimum current (critical current; $I_{\rm C}$) required to excite the stripe patterns is at a minimum [Fig. 2(f)]. For $\nu <$ (>) 2/3 , the stripes are in the excited, i.e., non-magnetic (ferromagnetic) phase [Figs. 2(a)−2(c) and 2(e)]. On either side of $\nu = 2/3$, $I_{\rm C}$ increases sharply; thus, $I_{\rm C}$ corresponds to the minimum energy required to flip a large amount of electron spins simultaneously to form the energetically unfavorable long-range-ordered structures.

R_{xx} enhancement caused by backscattering is known to be linked to nuclear spin polarization as mentioned above [8–10, 12, 15]. Thus, we performed optically detected microscopic NMR (OD-μ-NMR) to examine the relation between these stripe structures and $P_{\rm N}$. The μ-PL intensity was measured while irradiating the sample with continuous wave r.f. from a two-turn coil wrapped around the sample. The OD-μ-NMR [Fig. 3(a)] is the μ-PL intensity plotted as a function of the irradiating r.f. frequency. This spectrum measured in the ferromagnetic (non-magnetic) phase shows a clear resonant peak (dip) corresponding to ^{75}As nuclei [Fig. 3(a)]. The $\sim$ 5-kHz frequency difference between the peak and dip is caused by the difference in P between 1 and 0, respectively, which is consistent with the Knight shift obtained via resistively detected NMR [29]. The optically detected MRI (OD-MRI) image [Fig. 3(b)] shows the PL-intensity map corresponding to that collected during the *on*-resonant r.f. [Fig. 3(c)] minus that collected during the *off*-resonant r.f. [Fig. 3(d)]. In other words, this image displays the spatial distribution in the sizes of res-

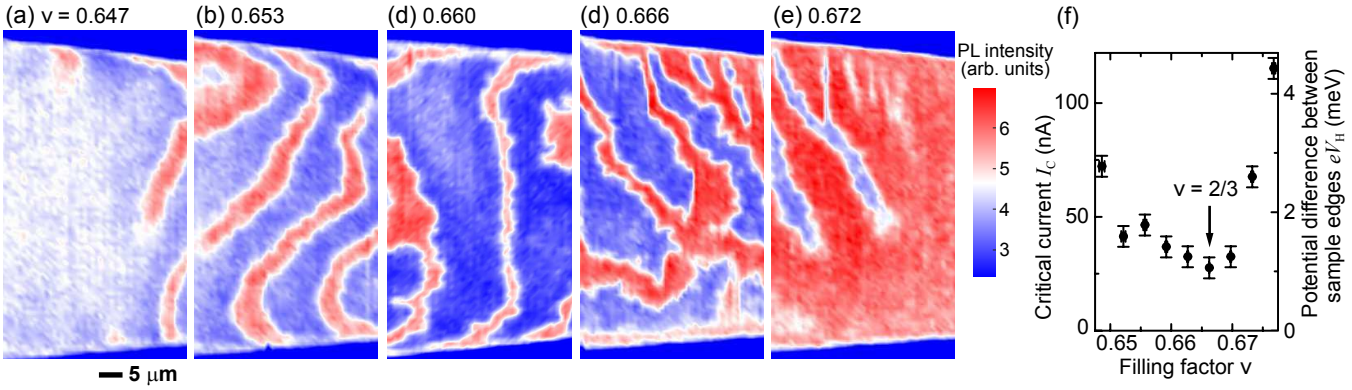

FIG. 2. (Color online) (a) to (e) 38× 68-μm^2 PL-intensity spatial images at ν of: (a) 0.647; (b) 0.653; (c) 0.660; (d) 0.666; and (e) 0.672, with $I_{SD} = 120$ nA. (f) Critical current at which first stripe becomes visible (I_C) as function of ν. Error in I_C determined by step size of applied current. Error in ν calculated from uncertainty in electron density. Right y-axis: Potential difference between sample edges, eV_H.

onant PL peak (green regions) and dip (orange region) occurring in the ferromagnetic and non-magnetic phases, respectively [Fig. 3(b)].

The PL images around $\nu = 2/3$ contain contributions from the spatial distributions of both P and P_N. To extract the contribution of P_N alone, we performed pump-probe imaging at $\nu = 0.5$, where P is homogeneously ~ 0.5 [12]. The pump-probe images shown in Figs. 4(a) and 4(b), were obtained via the following procedure: (i) The μ-PL collection spot was moved to an initial point; (ii) The pump condition was set ($\nu = 0.660$ for 4 min with $I_{SD} = 120$ nA); (iii) The μ-PL spectrum was obtained; (iv) The probe condition ($\nu = 1/2$ with $I_{SD} = 0$ nA) was set; (v) After 3 s, the μ-PL spectrum was obtained; and (vi) The collection spot was moved to the next point. We repeated this procedure while raster scanning the sample to construct the images under the pump [Fig. 4(a)] and probe [Fig. 4(b)] conditions. A stripe structure, which is generated by pumping the current at $I_{SD} = 120$ nA and $\nu = 0.660$ [Fig. 4(a)], remains visible 3 s after current deactivation ($I_{SD} = 0$) and changing to $\nu = 0.5$ [Fig. 4(b)]. Under this condition, P does not contribute significantly to the spatial pattern. Rather, the pattern seen here results from the remaining P_N. A sufficient pause with no current pumping causes the pattern to disappear [Fig. 4(c)]. The longitudinal relaxation time T_1 of the nuclear spins at $\nu = 0.5$ is estimated to be on the order of a minute, based on the PL time dependence measured at two fixed points in the two phases [Fig. 4(d)].

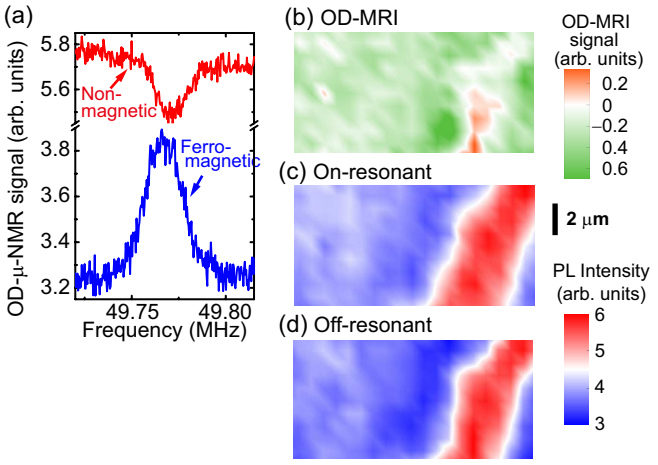

FIG. 3. (Color online) (a) Optically detected (OD)-μ-NMR spectra. (b) 15 × 7.5-μm^2 OD-MRI. PL-intensity spatial images under (c) on-resonant (49.7717 MHz) and (d) off-resonant r.f. (49.84 MHz). Data were obtained at $\nu = 0.660$ and $T = \sim 80$ mK. The r.f. power at the generator for both methods was −3.8 dBm.

Both OD-MRI and pump-probe imaging clearly show that the nuclear spins are polarized on both sides of the phase boundaries, but with opposite polarities. This asymmetry across the boundary is expected for forward-scattering electrons contributing to I_{SD} which flip their spins after crossing into an adjacent domain. We conclude, therefore, that P_N is parallel (anti-parallel) to B in the non-magnetic (ferromagnetic) phase. These images also reveal that P_N within ~ 5 μm of the boundary tends to be slightly, yet noticeably, stronger than that far from the boundary [Figs. 3(b) and 4(b)], a tendency clearly visible in many of the $\nu \sim 2/3$ PL images having stripes. We reason that this behavior is due to P_N diffusion with a typical diffusion length of $\sim 5 - 10$ μm. We cite the spatial distribution of P_N as likely having a stabilizing effect on the stripe shapes over time. The generation of P_N also modifies the electrochemical potential landscape via the Overhauser effect, which in turn modifies the rates of backscattering along the stripe boundaries.

The findings presented here give insight into the qual-

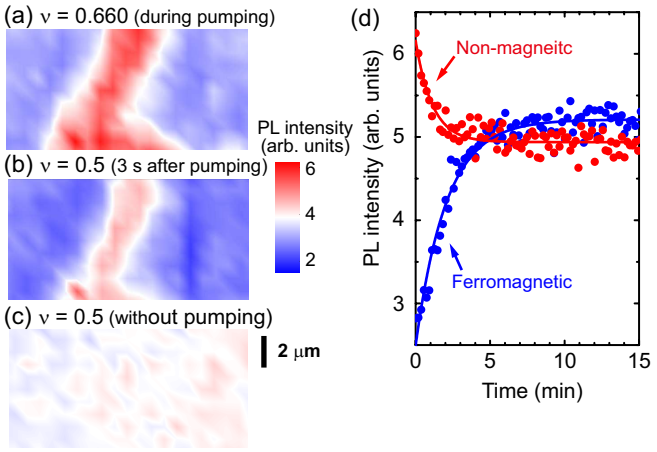

FIG. 4. (Color online) Pump-probe images and μ-PL intensity time evolution. (a) to (c) 15×7.5-μm^2-PL intensity spatial images at; (a) $\nu = 0.660$ during pumping, $I_{\rm SD} = 120$ nA; (b) $\nu = 0.5$ 3 s after pumping; and (c) $\nu = 0.5$, $I_{\rm SD} = 0$ nA. (d) PL intensity from two fixed points at (red) non-magnetic and (blue) ferromagnetic phases. $t = 0$: time when ν, $I_{\rm SD}$ were adjusted from pumping (0.660, 120 nA) to probing (0.5, 0 nA) conditions. Each data point in Fig. 4(d) was fitted using $a \exp \frac{t}{T_1} + b$, where $a = -2713.8$ (1216.5), $T_1 = 2.059$ (1.127) min, and $b = 5209.6$ (4938.8) for the ferromagnetic (non-magnetic) phase.

ities of dynamic nuclear polarization (DNP) generated in non-trivial FQH liquids. The important role of topological protection in non-equilibrium phenomena of these liquids is also illuminated. At the same time, this study offers a form of MRI which surpasses conventional techniques in its sensitivity to polarization magnitude and direction and its spatial resolution. We believe these findings and methods are directly relevant to efforts in quantum engineering based on DNP, and to topological materials, extending to fractional topological insulators [30] and topological quantum computation [31].

The authors are grateful to N. Shibata, K. Muraki, K. Nomura, N. Kumada, and T. Fujisawa for discussions, and to Y. Hirayama and M. Matsuura for experimental support. This work was supported by the Mitsubishi Foundation, and a Grant-in-Aid for Scientific Research (no. 24241039) from the Ministry of Education, Culture, Sports, Science, and Technology (MEXT), Japan. J.N.M. was supported by a Grant-in-Aid from MEXT and the Marubun Research Promotion Foundation. J. H. was supported by a Grant-in-Aid from the Tohoku University International Advanced Research and Education Organization.

* yusa@m.tohoku.ac.jp

[1] R. Tycko, S. E. Barrett, G. Dabbagh, L. N. Pfeiffer, and K. W. West, Science **268**, 1460 (1995).
[2] S. E. Barrett, G. Dabbagh, L. N. Pfeiffer, K. W. West, and R. Tycko, Phys. Rev. Lett. **74**, 5112 (1995).
[3] D. Gammon, S. W. Brown, E. S. Snow, T. A. Kennedy, D. S. Katzer, and D. Park, Science **277**, 85 (1997).
[4] N. N. Kuzma, P. Khandelwal, S. E. Barrett, L. N. Pfeiffer, and K. W. West, Science **281**, 686 (1998).
[5] J. M. Kikkawa and D. D. Awschalom, Science **287**, 473 (2000).
[6] G. Salis, D. T. Fuchs, J. M. Kikkawa, D. D. Awschalom, Y. Ohno, and H. Ohno, Phys. Rev. Lett. **86**, 2677 (2001).
[7] S. Kronmüler, W. Dietsche, J. Weis, K. von Klitzing, W. Wegscheider, and M. Bichler, Phys. Rev. Lett. **81**, 2526 (1998).
[8] S. Kronmüller, W. Dietsche, K. von Klitzing, G. Denninger, W. Wegscheider, and M. Bichler, Phys. Rev. Lett. **82**, 4070 (1999).
[9] J. H. Smet, R. A. Deutschmann, W. Wegscheider, G. Abstreiter, and K. von Klitzing, Phys. Rev. Lett. **86**, 2412 (2001).
[10] N. Freytag, Y. Tokunaga, M. Horvatić, C. Berthier, M. Shayegan, and L. P. Lévy, Phys. Rev. Lett. **87**, 136801 (2001).
[11] N. Kumada, K. Muraki, and Y. Hirayama, Science **313**, 329 (2006).
[12] L. Tiemann, G. Gamez, N. Kumada, and K. Muraki, Science **335**, 828 (2012).
[13] B. E. Kane, Nature **393**, 133 (1998).
[14] L. M. K. Vandersypen, M. Steffen, G. Breyta, C. S. Yannoni, M. H. Sherwood, and I. L. Chuang, Nature **414**, 883 (2001).
[15] G. Yusa, K. Muraki, K. Takashina, K. Hashimoto, and Y. Hirayama, Nature **434**, 1001 (2005).
[16] J. R. Petta, A. C. Johnson, J. M. Taylor, E. A. Laird, A. Yacoby, M. D. Lukin, C. M. Marcus, M. P. Hanson, and A. C. Gossard, Science **309**, 2180 (2005).
[17] F. H. L. Koppens, J. A. Folk, J. M. Elzerman, R. Hanson, L. H. Willems van Beveren, I. T. Vink, H. P. Tranitz, W. Wegscheider, L. P. Kouwenhoven, and L. M. K. Vandersypen, Science **309**, 1346 (2005).
[18] L. Childress, M. V. Gurudev Dutt, J. M. Taylor, A. S. Zibrov, F. Jelezko, J. Wrachtrup, P. R. Hemmer, and M. D. Lukin, Science **314**, 281 (2006).
[19] D. C. Tsui, H. L. Stormer, and A. C. Gossard, Phys. Rev. Lett. **48**, 1559 (1982).
[20] X. G. Wen, Phys. Rev. Lett. **64**, 2206 (1990).
[21] J. Hayakawa, K. Muraki, and G. Yusa, Nat. Nano. **8**, 31 (2013).
[22] See Supplemental Material on (i) experimental details, (ii) morphology reproducibility and potential landscape.
[23] G. Yusa, H. Shtrikman, and I. Bar-Joseph, Phys. Rev. Lett. **87**, 216402 (2001).
[24] A. Wójs, J. J. Quinn, and P. Hawrylak, Phys. Rev. B **62**, 4630 (2000).
[25] N. Shibata and K. Nomura, Phys. Soc. Jpn. **76**, 103711 (2007).
[26] S. Datta, *Electron Transport in Mesoscopic Systems* (Cambridge Univ. Press, Cambridge, 1995).
[27] A. Bid, N. Ofek, H. Inoue, M. Heiblum, C. L. Kane, V. Umansky, and D. Mahalu, Nature **466**, 585 (2010).
[28] Y.-H. Wu, G. J. Sreejith, and J. K. Jain, Phys. Rev. B **86**, 115127 (2012).
[29] G. Yusa, N. Kumada, K. Muraki, and Y. Hirayama, arXiv:cond-mat

http://arxiv.org/abs/cond-mat/0510310 (2005).
[30] M. Levin and A. Stern, Phys. Rev. Lett. **103**, 196803 (2009).
[31] A. Y. Kitaev, Ann. Phys. **303**, 2 (2003).